Mitochondrial Morphofunctional Profiling in Primary Human Skin Fibroblasts Using TMRM and Mitotracker Green Co-staining

Methods in molecular biology (Clifton, N.J.)

Bergmans, Jesper M.M.; van de Westerlo, Els M.A.; Grefte, Sander; Adjobo-Hermans, Merel J.W.; Koopman, Werner J.H.

https://doi.org/10.1007/978-1-0716-4264-1_12

Chapter 12

Mitochondrial Morphofunctional Profiling in Primary Human Skin Fibroblasts Using TMRM and Mitotracker Green Co-staining

Jesper M. M. Bergmans, Els M. A. van de Westerlo, Sander Grefte, Merel J. W. Adjobo-Hermans, and Werner J. H. Koopman

Abstract

Mitochondrial morphology and membrane potential ($\Delta\psi$) are important readouts of mitochondrial function. Integrated analysis of these parameters in living cells can be performed using fluorescent lipophilic cations, which enter cells and accumulate in the mitochondrial matrix in a $\Delta\psi$-dependent manner. Here, we describe the use of tetramethylrhodamine methyl ester (TMRM) and Mitotracker Green FM (MG) for mitochondrial morphology and semiquantitative $\Delta\psi$ analysis in living primary human skin fibroblasts (PHSFs). Practically, we present an integrated protocol to quantify mitochondrial morphology parameters and signal intensity using epifluorescence microscopy of PHSFs co-stained with TMRM and MG. This approach performs best using large flat cells like PHSFs, which display a high mitochondria-specific fluorescence signal and are imaged at a relatively high (x40) magnification.

Key words TMRM, Mitotracker Green, FCCP, Mitochondrial morphology

1 Introduction

Alterations in mitochondrial morphology are intricately linked to changes in mitochondrial function and vice versa, giving rise to the concept of mitochondrial "morphofunction" [1–3]. An important functional readout is the inside-negative electrical potential ($\Delta\psi$) across the mitochondrial inner membrane (MIM). Here we describe an automated approach for quantification of mitochondrial morphology and $\Delta\psi$ using the fluorescent cations tetramethylrhodamine methyl ester (TMRM) and Mitotracker Green FM (MG) in co-stained living primary human skin fibroblasts (PHSFs). This strategy is based upon our previous PHSF studies (e.g., [4–12]). TMRM and MG accumulate in the mitochondrial matrix [13–20] in a manner dependent on the electrical potential (ΔV) across the plasma membrane (PM) and the electrical potential

Carlos M. Palmeira and Paulo J. Oliveira (eds.), *Mitochondrial Bioenergetics: Methods and Protocols*, Methods in Molecular Biology, vol. 2878, https://doi.org/10.1007/978-1-0716-4264-1_12,

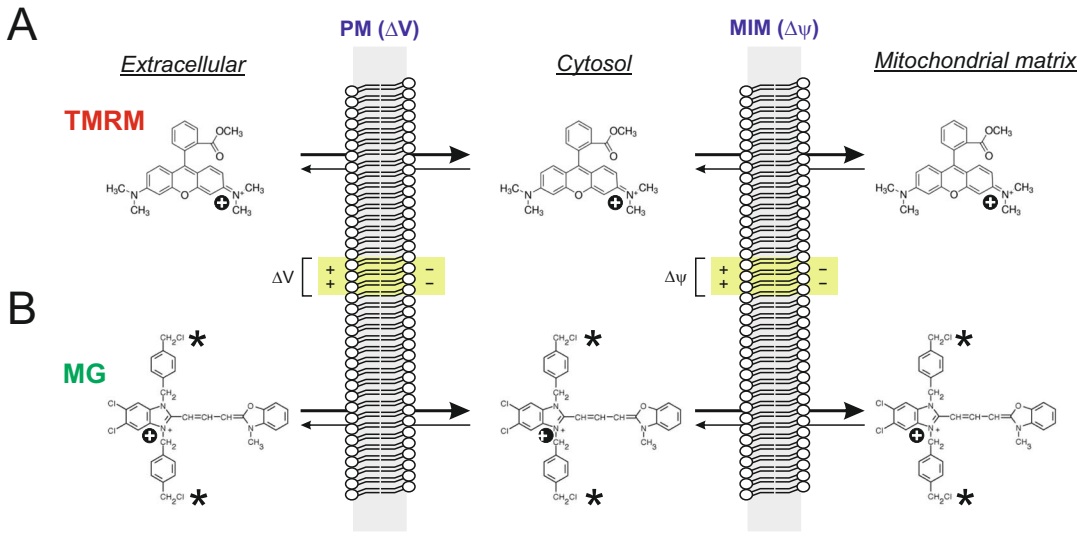

Fig. 1 Chemical structure and principle of mitochondrial TMRM and MG staining. (**a**) Mechanism of accumulation of TMRM in the cytosol (driven by the plasma membrane electrical potential; ΔV) and mitochondrial matrix (driven by the MIM membrane potential; Δψ). The molecular movement of TMRM through the PM and MIM is indicated by arrows (thicker arrows indicate the magnitude of this movement). The positive charge of TMRM is marked by a black circular "+" symbol. (**b**) Same as panel A, but now for MG. The two thiol-reactive chloromethyl groups are indicated asterisks. *Abbreviations*: *ΔV* plasma membrane electrical potential, *Δψ* trans-MIM electrical potential, *MIM* mitochondrial inner membrane, *PM* plasma membrane

(Δψ) across the mitochondrial inner membrane (MIM; Fig. 1). This behavior is quantitatively described by: $C_m = C_{ext} \cdot EXP\{-[((\Delta V + \Delta\psi) \cdot zF)/RT]\}$, where C_m is the mitochondrial matrix concentration of the cation, C_{ext} is the extracellular concentration of the cation, *z* is the charge of the cation, F is Faraday's constant, R is the ideal gas constant and T is the absolute temperature [8, 21–23]. Assuming that Δψ equals about 120–180 mV, TMRM and MG accumulate between 100- and 1000-fold in the mitochondrial matrix [21, 24]. This means that, in absence of ΔV changes, the mitochondrial fluorescence signals of TMRM and MG represent a semi-quantitative readout of Δψ. Importantly, comparative analysis of rhodamine 123 (R123), tetramethylrhodamine ethyl ester (TMRE), and TMRM demonstrated that the fluorescence of these cations is quenched upon reaching high C_m values [16, 25, 26]. This means that C_{ext} should be kept relatively low (i.e., nM concentrations) for C_m to increase upon Δψ hyperpolarization. In case of MG, the impact of Δψ depolarization on its mitochondrial localization is reduced by the presence of two chloromethyl (CM) groups (Fig. 1), which can react with accessible nucleophiles (e.g., thiol groups of peptides and proteins), thereby forming an aldehyde-fixable conjugate [27].

2 Materials

2.1 Cells

1. Primary human skin fibroblasts (PHSFs).

2.2 Medium

1. Medium 199 (M199; Invitrogen, Life Technologies Europe BV, Bleiswijk, Netherlands), 10% Fetal bovine serum, 1% Penicillin/streptomycin.

2.3 Solutions

1. Dimethyl sulfoxide (DMSO).

2.4 Reagents

1. Tetramethylrhodamine methyl ester (TMRM; Thermo-Fisher Scientific, Landsmeer, The Netherlands).
2. Mitotracker Green FM (MG; Thermo-Fisher).

2.5 Instruments and Equipment

1. Axiovert 200 M inverted microscope (Carl Zeiss AG, Oberkochen, Germany) equipped with [28].
   (a) Plan NeoFluar objective (x63, 1.25 Numerical Aperture [NA]; Carl Zeiss).
   (b) Xenon lamp-based monochromator (Polychrome IV) with a spectral bandwidth of 15 nM (TILL Photonics, Gräfelfing, Germany).
   (c) Motorized dichroic mirrors (Omega Optical Inc., Brattleboro, VT, USA).
   (d) Motorized filter wheel (Sutter Instrument Company, Novato, CA, USA).
   (e) CoolSNAP HQ monochrome CCD-camera (Roper Scientific, Evry Cedex, France).
   (f) Environmental control system (Carl Zeiss).

2.6 Software

1. MetaFluor 6.1 software (Molecular Devices Corporation, Downingtown, PA, USA).
2. Image Pro Plus software (Media Cybernetics, Rockville, MD, USA).
3. Origin Pro software (Originlab Corp., Northampton, MA, USA).

3 Methods

3.1 Cell Staining and Epifluorescence Microscopy Imaging

1. Seed the cells at a density of 100,000 cells on glass coverslips (Ø 24 mm; placed in a 6-well plate).
2. Culture the cells during 24 h in M199 to ~70% confluence in a humidified atmosphere (95% air, 5% CO_2, 37 °C).

3. Dissolve TMRM and MG in DMSO and prepare M199 containing 15 nM TMRM and 50 nM MG.
4. Stain the cells during 25 min in M199 containing 15 nM TMRM and 50 nM MG (37 °C in 95% air, 5% CO_2, dark). At this concentration, TMRM operates in the non-quenching mode [26, 29, 30].
5. Wash the cells twice with PBS.
6. Mount the coverslip with the cells on the microscope.
7. Replace the PBS by M199 culture medium.
8. Excite TMRM and MG at 540 and 488 nM, respectively. In combination with the used dichroic mirrors and fluorescence emission filters see [31], spectral bleedthrough between TMRM and MG emission signals is prevented.
9. Select a field of view (FOV) and acquire a single TMRM and MG image.
10. Select a next adjacent FOV and acquire the next TMRM and MG image.
11. Repeat step 9 until a total of 20–30 images have been acquired.
12. To obtain enough statistical power, perform N = 3 independent experiments (days), yielding 60–90 images for analysis.

3.2 Image Processing and Quantification of Mitochondrial Morphology

Mitochondrial morphology parameters and fluorescence intensity are obtained by image quantification following application of an image processing pipeline. The ultimate goal of this pipeline is to generate a segmented binary (BIN) image, in which mitochondrial objects are depicted as white objects on a black background. Obtaining a proper BIN image requires that [10, 28] (**a**) the mitochondria-specific TMRM and MG signals are high enough, (**b**) the image is relatively noise-free (e.g., contains few noise-related pixels due to defocusing, which will introduce artifacts during image processing), and (**c**) true mitochondrial objects consists of enough pixels. Although the protocol provided below was designed for use with dedicated software, its implementation in other (open-source) software is relatively straightforward.

1. Open a 16-bit TMRM image (RAW) in the Image Pro Plus software (Fig. 2a; RAW).
2. Perform a background correction (Fig. 2a; marked: "B" in the RAW image) by subtracting the intensity (gray value) in an extracellular region of interest (ROI).
3. This yields a 16-bit background-corrected image.
4. Convert the 16-bit image into an 8-bit image using best-fit rescaling (Fig. 2a; COR).
5. Apply a linear contrast stretch (LCS) operation (Fig. 2a; LCS).

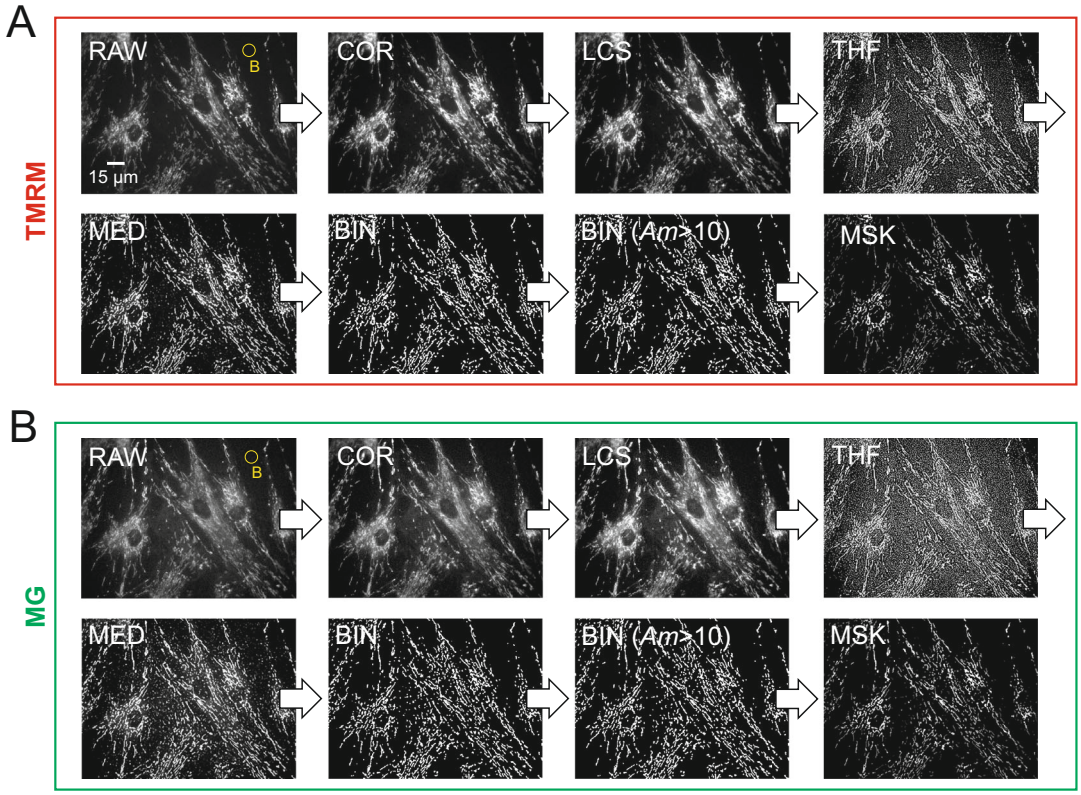

Fig. 2 Analysis of mitochondrial morphology and fluorescence intensity in cells co-stained with TMRM and MG. Primary human skin fibroblasts (PHSFs) were co-stained with TMRM and MG and visualized using epifluorescence microscopy. Image processing was applied to extract numerical information on mitochondrial morphology and staining intensity from the fluorescence images. (**a**) TMRM image processing pipeline. Microscopy images (RAW) were background-corrected using an extracellular region of interest (ROI; yellow; marked "B"), yielding a corrected (COR) image. The latter was subsequently processed using a linear contrast stretch (LCS), top-hat filtering (THF) and median filtering (MED). The MED image was intensity-thresholded, yielding a black-and-white binary (BIN) image, representing white TMRM-positive objects on a black background. To reduce noise, small objects with a size (*Am*) below 10 pixels were removed (BIN ($Am > 10$) image). Finally, the BIN ($Am > 10$) image was used to mask the COR image using a Boolean "AND" operation, resulting in a masked (MSK) image. (**b**) Image processing pipeline applied to the MG fluorescence images (identical to panel **a**). In this figure, images were contrast-optimized for visualization purposes

6. Apply a top-hat filter (THF) using a 7 × 7 kernel, 3 passes and a strength of 3 (Fig. 2a; THF).
7. Apply a median filter (MED) using a 3 × 3 kernel and 8 passes (Fig. 2a; MED).
8. Apply an intensity threshold (T) operation using a gray value of 128, yielding an 8-bit binary (BIN) image highlighting mitochondrial objects (white) on a black background (Fig. 2a; BIN).

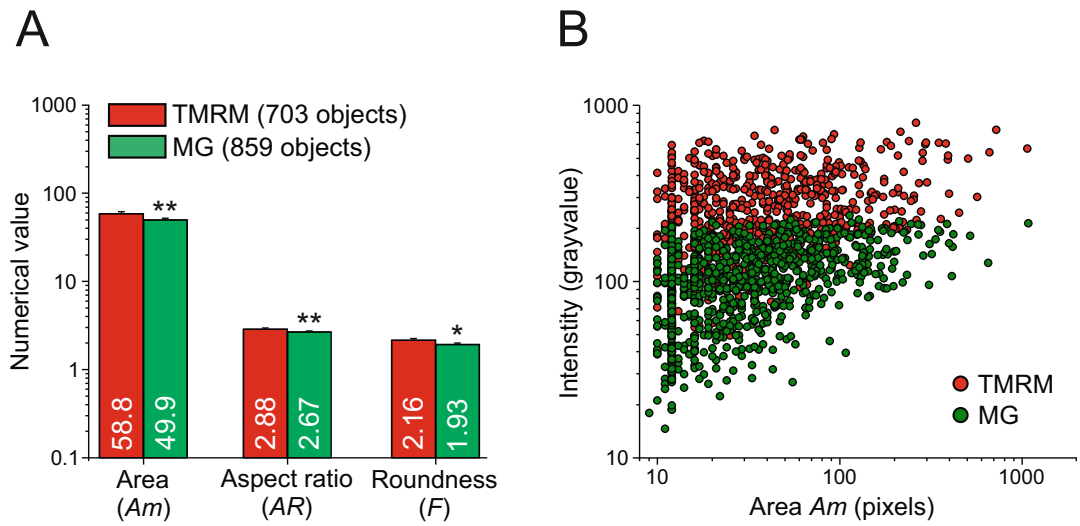

Fig. 3 Example of monovariate and bivariate descriptor visualization. (**a**) Example of monovariate analysis. Mean descriptor values (error bars reflect the standard error of the mean; SEM) obtained from the MSK images for TMRM (Fig. 2a; 703 objects) and MG (Fig. 2b; 859 objects). Depicted are mitochondrial area (*Am*, in pixels; a measure of mitochondrial size), mitochondrial aspect ratio (*AR*, a measure of mitochondrial length) and mitochondrial formfactor (*F*; a combined measure of mitochondrial length and degree of branching). Statistical analysis (Mann-Whitney test) revealed significant differences between the TMRM- and MG-reported values (given by numerals in each bar). (**b**) Example of bivariate analysis. Relationship between mitochondrial area *Am* and fluorescence intensity derived from the MSK images for TMRM (Fig. 2a) and MG (Fig. 2b). Each symbol reflects an individual TMRM (red) or MG (green) fluorescent object. A linear fit revealed a significant positive correlation ($p < 0.001$) between *Am* and intensity for TMRM (slope $= 0.54 \pm 0.059$(SE)) and MG (slope $= 0.24 \pm 0.022$(SE))

9. To remove non-mitochondrial objects introduced by the THF filter, only white objects with an area (Am) > 10 pixels were included in the analysis (Fig. 2a; BIN($Am > 10$)).
10. Mask the 16-bit COR images with the 8-bit BIN image to yield "masked" (Fig. 2a; MSK) images by applying a Boolean operation (COR(AND)BIN).
11. Repeat **steps 1–10** for the next TMRM image.
12. MG images (RAW) are processed identically to TMRM images (Fig. 2b).

The obtained MSK images can now be analyzed by quantifying the properties of each individual TMRM or MG-positive object. This yields the fluorescence intensity (Dm; gray value) of each individual object, as well as the total number of objects per FOV. The latter can be divided by the number of cells within the FOV to obtain the approximate number of mitochondrial objects per cell (Nc). Other descriptors include the area of the individual fluorescent objects (A_m; in pixels), the aspect ratio of the objects (AR; being the ratio between the major and minor axis of the ellipse

equivalent to the object), and the formfactor (*F*) of the objects. Lower and higher values of *AR* and *F* correspond to more circular and more elongated/branched morphologies, respectively. Given their extremely flat morphology [6], the product of *Am* and *Nc* can be computed at the level of individual cells or FOVs to obtain a measure of mitochondrial mass (*Mm*). Data can be visualized in a monovariate manner (Fig. 3a), for instance as the mean value for a (collection of) FOV(s), or for individual objects to allow bivariate analysis (Fig. 3b). The obtained data is also compatible with multivariate analyses including Principal Component Analysis (PCA), cluster analysis, and machine learning approaches (e.g., [10, 32, 33]).

4 Notes

1. Changes in mitochondrial TMRM or MG fluorescence intensity (suggestive of changes in $\Delta\psi$) should ideally be accompanied by control experiments ruling out changes in ΔV [34], for instance by electrophysiological analysis [35].
2. Mitochondrial imaging should be carried out using short illumination times and low illumination intensities to prevent phototoxicity and light-induced TMRM-mediated opening of the mitochondrial permeability transition pore (e.g., [30, 31, 36–38]). This also minimizes induction of photobleaching-related artifacts. In this context, placing neutral density (ND) filters in the excitation light path can be useful.
3. To prevent artifacts induced by mitochondrial movement during acquisition of individual images, experiments can be conducted at a lower temperature (e.g., at 20 °C instead of 37 °C).
4. To prevent saturation of the fluorescence signal, it recommended that this signal is substantially below the maximum gray value allowed by the CCD camera.
5. Due to potential biological variability it is advisable to always include the same reference cell line in all experiments (analyzed on the same day) for data normalization purposes and quality control analysis (*for* details see: [10]).

Acknowledgements

WJHK is supported by the Next Level Animal Sciences (NLAS) initiative ("Data and Models") of the Wageningen University (Wageningen, The Netherlands) and by Radboudumc Principal Investigator (PI) funding (Nijmegen, The Netherlands). We thank S. Lauwen (Dept. of Medical BioSciences, Radboud

University Medical Center, Nijmegen, The Netherlands) for performing microscopy experiments. *JB* is supported by an EJP-RD grant ("CureMILS") through ZonMW (Netherlands Organisation for Health Research and Development; #463003001).

Potential Conflict of Interest *WJHK* is an ad-hoc scientific advisor of Khondrion B.V. (Nijmegen, The Netherlands). This SME had no involvement in the data collection, analysis and interpretation, writing of the manuscript, and in the decision to submit the manuscript for publication.

References

1. Benard G, Rossignol R (2008) Ultrastructure of the mitochondrion and its bearing on function and bioenergetics. Antioxid Redox Signal 10(8):1313–1342. https://doi.org/10.1089/ars.2007.2000
2. Willems PHGM, Rossignol R, Dieteren CE, Murphy MP, Koopman WJH (2015) Redox homeostasis and mitochondrial dynamics. Cell Metab 22(2):207–218. https://doi.org/10.1016/j.cmet.2015.06.006
3. Bulthuis EP, Adjobo-Hermans MJW, Willems PHGM, Koopman WJH (2019) Mitochondrial morphofunction in mammalian cells. Antioxid Redox Signal 30(18):2066–2109. https://doi.org/10.1089/ars.2018.7534
4. Koopman WJH, Verkaart S, Visch HJ, van der Westhuizen FH, Murphy MP, van den Heuvel LW, Smeitink JA, Willems PH (2005a) Inhibition of complex I of the electron transport chain causes O2-. -mediated mitochondrial outgrowth. Am J Physiol Cell Physiol 288(6): C1440–C1450. https://doi.org/10.1152/ajpcell.00607.2004
5. Koopman WJH, Visch HJ, Verkaart S, van den Heuvel LW, Smeitink JA, Willems PH (2005b) Mitochondrial network complexity and pathological decrease in complex I activity are tightly correlated in isolated human complex I deficiency. Am J Physiol Cell Physiol 289(4): C881–C890. https://doi.org/10.1152/ajpcell.00104.2005
6. Koopman WJH, Visch HJ, Smeitink JA, Willems PH (2006) Simultaneous quantitative measurement and automated analysis of mitochondrial morphology, mass, potential, and motility in living human skin fibroblasts. Cytometry A 69(1):1–12. https://doi.org/10.1002/cyto.a.20198
7. Distelmaier F, Koopman WJH, Testa ER, de Jong AS, Swarts HG, Mayatepek E, Smeitink JA, Willems PH (2008) Life cell quantification of mitochondrial membrane potential at the single organelle level. Cytometry A 73(2): 129–138. https://doi.org/10.1002/cyto.a.20503
8. Koopman WJH, Distelmaier F, Esseling JJ, Smeitink JA, Willems PH (2008) Computer-assisted live cell analysis of mitochondrial membrane potential, morphology and calcium handling. Methods 46(4):304–311. https://doi.org/10.1016/j.ymeth.2008.09.018
9. Willems PHGM, Smeitink JAM, Koopman WJH (2009) Mitochondrial dynamics in human NADH:ubiquinone oxidoreductase deficiency. Int J Biochem Cell Biol 41(10): 1773–1782. https://doi.org/10.1016/j.biocel.2009.01.012
10. Iannetti EF, Smeitink JAM, Beyrath J, Willems PHGM, Koopman WJH (2016) Multiplexed high-content analysis of mitochondrial morphofunction using live-cell microscopy. Nat Protoc 11(9):1693–1710. https://doi.org/10.1038/nprot.2016.094
11. Teixeira J, Basit F, Willems PHGM, Wagenaars JA, van de Westerlo E, Amorim R, Cagide F, Benfeito S, Oliveira C, Borges F, Oliveira PJ, Koopman WJH (2021) Mitochondria-targeted phenolic antioxidants induce ROS-protective pathways in primary human skin fibroblasts. Free Radic Biol Med 163:314–324. https://doi.org/10.1016/j.freeradbiomed.2020.12.023
12. Bulthuis EP, Einer C, Distelmaier F, Groh L, van Emst-de Vries SE, van de Westerlo E, van de Wal M, Wagenaars J, Rodenburg RJ, Smeitink JAM, Riksen NP, Willems PHGM, Adjobo-Hermans MJW, Zischka H, Koopman WJH (2022) The

decylTPP mitochondria-targeting moiety lowers electron transport chain supercomplex levels in primary human skin fibroblasts. Free Radic Biol Med 188:434–446. https://doi.org/10.1016/j.freeradbiomed.2022.06.011

13. Ehrenberg B, Montana V, Wei MD, Wuskell JP, Loew LM (1988) Membrane potential can be determined in individual cells from the nernstian distribution of cationic dyes. Biophys J 53(5):785–794. https://doi.org/10.1016/S0006-3495(88)83158-8
14. Floryk D, Houstěk J (1999) Tetramethyl rhodamine methyl ester (TMRM) is suitable for cytofluorometric measurements of mitochondrial membrane potential in cells treated with digitonin. Biosci Rep 19(1):27–34. https://doi.org/10.1023/a:1020193906974
15. Haugland RP (1999) Handbook of fluorescent probes and research chemicals. Molecular Probes, Eugene
16. Scaduto RC Jr, Grotyohann LW (1999) Measurement of mitochondrial membrane potential using fluorescent rhodamine derivatives. Biophys J 76(1 Pt 1):469–477. https://doi.org/10.1016/S0006-3495(99)77214-0
17. Buckman JF, Hernández H, Kress GJ, Votyakova TV, Pal S, Reynolds IJ (2001) MitoTracker labeling in primary neuronal and astrocytic cultures: influence of mitochondrial membrane potential and oxidants. J Neurosci Methods 104(2):165–176. https://doi.org/10.1016/S0165-0270(00)00340-X
18. Lemasters JJ, Ramshesh VK (2007) Imaging of mitochondrial polarization and depolarization with cationic fluorophores. Methods Cell Biol 80:283–295. 10.101
19. Cottet-Rousselle C, Ronot X, Leverve X, Mayol JF (2011) Cytometric assessment of mitochondria using fluorescent probes. Cytometry A 79(6):405–425. https://doi.org/10.1002/cyto.a.21061
20. Perry SW, Norman JP, Barbieri J, Brown EB, Gelbard HA (2011) Mitochondrial membrane potential probes and the proton gradient: a practical usage guide. BioTechniques 50(2):98–115. https://doi.org/10.2144/000113610
21. Ross MF, Kelso GF, Blaikie FH, James AM, Cochemé HM, Filipovska A, Da Ros T, Hurd TR, Smith RA, Murphy MP (2005) Lipophilic triphenylphosphonium cations as tools in mitochondrial bioenergetics and free radical biology. Biochemistry (Mosc) 70(2):222–230. https://doi.org/10.1007/s10541-005-0104-5
22. Nicholls DG, Ward MW (2000) Mitochondrial membrane potential and neuronal glutamate excitotoxicity: mortality and millivolts. Trends Neurosci 23(4):166–174. https://doi.org/10.1016/S0166-2236(99)01534-9
23. Farkas DL, Wei MD, Febbroriello P, Carson JH, Loew LM (1989) Simultaneous imaging of cell and mitochondrial membrane potentials. Biophys J 56(6):1053–1069. https://doi.org/10.1016/S0006-3495(89)82754-7
24. Murphy MP, Smith RA (2000) Drug delivery to mitochondria: the key to mitochondrial medicine. Adv Drug Deliv Rev 41(2):235–250. https://doi.org/10.1016/S0169-409X(99)00069-1
25. Monteith A, Marszalec W, Chan P, Logan J, Yu W, Schwarz N, Wokosin D, Hockberger P (2013) Imaging of mitochondrial and non-mitochondrial responses in cultured rat hippocampal neurons exposed to micromolar concentrations of TMRM. PLoS One 8(3):e58059. https://doi.org/10.1371/journal.pone.0058059
26. Esteras N, Adjobo-Hermans MJW, Abramov AY, Koopman WJH (2020) Visualization of mitochondrial membrane potential in mammalian cells. Methods Cell Biol 155:221–245. https://doi.org/10.1016/bs.mcb.2019.10.003
27. Poot M, Zhang YZ, Krämer JA, Wells KS, Jones LJ, Hanzel DK, Lugade AG, Singer VL, Haugland RP (1996) Analysis of mitochondrial morphology and function with novel fixable fluorescent stains. J Histochem Cytochem 44(12):1363–1372. https://doi.org/10.1177/44.12.8985128
28. Nooteboom M, Forkink M, Willems PHGM, Koopman WJH (2012) Live-cell quantification of mitochondrial functional parameters. In: Badoer E (ed) Visualization techniques: from immunochemistry to magnetic resonance imaging, Neurometh, vol 70, pp 111–127. https://doi.org/10.1007/978-1-61779-897-9_6
29. Ward MW (2010) Quantitative analysis of membrane potentials. Methods Mol Biol 591:335–351. https://doi.org/10.1007/978-1-60761-404-3_20
30. Sambri I, Massa F, Gullo F, Meneghini S, Cassina L, Carraro M, Dina G, Quattrini A, Patanella L, Carissimo A, Iuliano A, Santorelli F, Codazzi F, Grohovaz F, Bernardi P, Becchetti A, Casari G (2020) Impaired flickering of the permeability transition pore causes SPG7 spastic paraplegia. EBioMedicine 61:103050. https://doi.org/10.1016/j.ebiom.2020.103050

31. Desai S, Grefte S, van de Westerlo E, Lauwen S, Paters A, Prehn JHM, Gan Z, Keijer J, Adjobo-Hermans MJW, Koopman WJH (2024) Performance of TMRM and Mitotrackers in mitochondrial morphofunctional analysis of primary human skin fibroblasts. Biochim Biophys Acta Bioenerg 1865(2):149027. https://doi.org/10.1016/j.bbabio.2023.149027
32. Blanchet L, Buydens MC, Smeitink JA, Willems PH, Koopman WJH (2011) Isolated mitochondrial complex I deficiency: explorative data analysis of patient cell parameters. Curr Pharm Des 17(36):4023–4033. https://doi.org/10.2174/138161211798764870
33. Blanchet L, Smeitink JA, van Emst-de Vries SE, Vogels C, Pellegrini M, Jonckheere AI, Rodenburg RJ, Buydens LM, Beyrath J, Willems PH, Koopman WJH (2015) Quantifying small molecule phenotypic effects using mitochondrial morpho-functional fingerprinting and machine learning. Sci Rep 5:8035. https://doi.org/10.1038/srep08035
34. Nicholls DG (2006) Simultaneous monitoring of ionophore- and inhibitor-mediated plasma and mitochondrial membrane potential changes in cultured neurons. J Biol Chem 281(21):14864–14874. https://doi.org/10.1074/jbc.M510916200
35. Forkink M, Manjeri GR, Liemburg-Apers DC, Nibbeling E, Blanchard M, Wojtala A, Smeitink JA, Wieckowski MR, Willems PH, Koopman WJH (2014) Mitochondrial hyperpolarization during chronic complex I inhibition is sustained by low activity of complex II, III, IV and V. Biochim Biophys Acta 1837(8):1247–1256. https://doi.org/10.1016/j.bbabio.2014.04.008
36. Falchi AM, Isola R, Diana A, Putzolu M, Diaz G (2005) Characterization of depolarization and repolarization phases of mitochondrial membrane potential fluctuations induced by tetramethylrhodamine methyl ester photoactivation. FEBS J 272(7):1649–1659. https://doi.org/10.1111/j.1742-4658.2005.04586.x
37. Blanchet L, Grefte S, Smeitink JA, Willems PH, Koopman WJH (2014) Photo-induction and automated quantification of reversible mitochondrial permeability transition pore opening in primary mouse myotubes. PLoS One 9(11):e114090. https://doi.org/10.1371/journal.pone.0114090
38. Basit F, van Oppen LM, Schöckel L, Bossenbroek HM, van Emst-de Vries SE, Hermeling JC, Grefte S, Kopitz C, Heroult M, Hgm Willems P, Koopman WJH (2017) Mitochondrial complex I inhibition triggers a mitophagy-dependent ROS increase leading to necroptosis and ferroptosis in melanoma cells. Cell Death Dis 8(3):e2716. https://doi.org/10.1038/cddis.2017.133